Pergamon

Cement and Concrete Research 32 (2002) 1831–1838

CEMENT AND CONCRETE RESEARCH

Microconcrete ageing ultrasonic identification

M. Panet[a,*], C. Cheng[b], M. Deschamps[c], O. Poncelet[c], B. Audoin[c]

[a]EDF R&D MMC MTC1, Départment de Mécanique et Technologie des Composants, 77818 Moret/Loing, France
[b]Université des Sciences et Technologies, Chengdu, China
[c]Laboratoire de Mécanique Physique, Université de Bordeaux 1, 33405 Talence, France

Received 25 May 2001; accepted 28 May 2002

Abstract

In this paper, a global identification of the Voigt stiffness matrix is provided for different aged microconcrete. The approach is a part of the research that develops actively the field of cement-based materials ageing assessment. It investigates the ability of the ultrasonic and laser impact tests to classify the ageing level of the altered specimen and to obtain an evaluation of elasticity coefficients. Three different specimens are tested: the first one with no degradation is used as the reference and the other two are damaged by using freeze/thaw cycles or a chemical attack. The ageing provides a heterogeneous structure, which is approximated like an equivalent weakly transversely isotropic medium in the long wave length limit hypothesis. To validate qualitatively the porosity and water content influences on the elasticity moduli, the experimental results are compared with the prediction of the Hudson's homogenized scattering medium. This model is extended to a smooth phenomenological law in the domain of high porosity. The interest of modelling a continuously altered medium is finally outlined and opens a field of investigation in the future, which accounts for the local properties of heterogeneous materials, improving the ultrasonic inspection.

Keywords: Ageing; Porosity; Ultrasonic; Mortar; Concrete

1. Introduction

The ageing of civil engineering structures is supported by a sustained research, to know how the physical and mechanical properties of concrete evolute, when an external alteration damages progressively the material cohesion. Extensive ageing experiments [1,2] show that ageing can induce a microstructure transformation. At a macroscopic scale, ageing corresponds with an increase of the porosity. It is induced either by a ionic transport within the cement paste, which is governed by a chemical diffusion process, or by the pore volume expansion when ice develops during freezing. The material softening is generally inspected by the ultrasonic nondestructive method, which has been applied previously in the field of composite and heterogeneous materials [3–5]. The former works investigate the bulk wave velocity and indicate the sensitivity of the wave propagation with the porosity evolution and the crack orientation [6]. To quantify the physical alteration of the cement paste around the aggregates and validate mechanical models, the dissipative properties began to be examined by means of surface wave attenuation and dispersive media [7].

The aim of this paper is to confirm that the identification of the mechanical behaviour of a cement-based material by means of the wave propagation analysis is still an open question, especially when industrial applications are considered. It reports the results of a robust identification procedure successfully applied formerly in the field of homogeneous composite materials [8]. The objective is mainly to identify the influences of the porosity and water content on the stiffness constants of differently altered microconcrete prisms. Using ultrasonic measurements in the frame of the underlying homogenization assumption, the elastic constants are obtained from the waves first arrival time experimental chronometry. The laboratory accounts for the recent developments of both ultrasonic transmission and low-energy impact laser equipment. The superficial altered layer of a sample is identified by the laser-generated Rayleigh

* Corresponding author. Tel.: +33-1-60-73-64-85; fax: +33-1-60-73-65-59.
E-mail address: michel.panet@edf.fr (M. Panet).

0008-8846/02/$ – see front matter © 2002 Published by Elsevier Science Ltd.
PII: S0008-8846(02)00885-2

Table 1
Microconcrete mixture and unhydrated cement Fluo X

Material	Cement	Sand Sika			Water	Unhydrated cement	
Class	CEM I 42.5	0.5–1.6 mm	1–3.2 mm	2–4 mm		SiO_2	20.1
kg/m^3	530	727	291	436	265	Al_2O_3	5.0
Ratio	water/cement = 0.5, cement/sand = 0.3					Fe_2O_3	3.1
Rc28 = – 35.6 MPa, slump = 10.5 cm						CaO	60.9
						SO_3	3.1

wave detection. Experimental data of ultrasonic transmission tests are treated with the inverse resolution algorithm of the Christoffel equation to identify the material stiffness matrix and an accuracy confidence interval deducts from the error statistical distribution of the stiffness coefficients. Hudson's [9] model is then applied to evaluate the observed influence of the porosity and of the water content on the identified parameters.

2. Microconcrete specimens

The specimens are sized $50 \times 150 \times 300$ mm. Formulation is defined at Table 1. The sand sieving defines a regular distribution of granular silica inclusions (Fig. 1). The maximal diameter is near two half the time smaller than the slowest shear wavelength of 10 mm at 250 kHz. It makes the material homogeneous for the ultrasonic wave propagation, but the higher frequency components of the laser-induced waves may be filtered by the scattering on the aggregate particles.

A first series of 10 bars is aged by rapid freeze/thaw cycles at the Norwegian Building Research Institute [10]. The procedure is the ASTM C666. Fourteen cycles are applied, with a cooling rate approximately 12° C/h in the limit $+5/-18$ °C. A crack mapping is obtained by impregnating with a fluorescent liquid the middle specimen 50×150 mm cross-section on frost-induced cracks. The resulting 50×150 mm^2 plane section at 100 mm from the prism end was analysed in ultraviolet light microscope. Mainly, four cracks 50 mm long parallel to the 150 mm sides were counted, and a net of intersecting traverses was counted in bond zone between cement paste and aggregate particles.

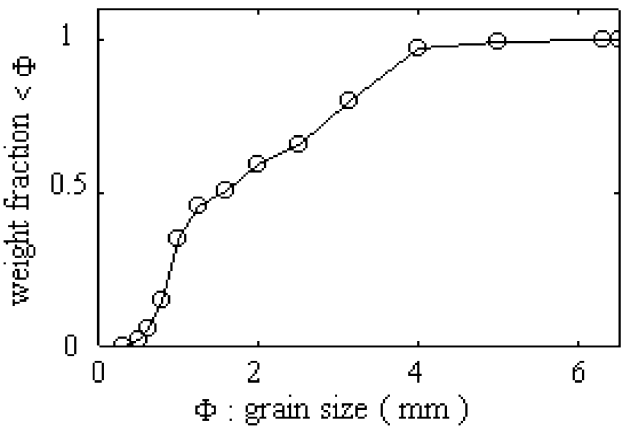

Fig. 1. Sand granularity.

The crack density is higher in a 3 mm thick layer, where the cracks orientate parallel to the surface of the samples. The relative modulus close 0.40–0.50 is calculated by the square resonance frequencies ratio of the aged/unaged microconcrete specimens using a light tapping test applied to the 150×300 mm side of the samples. This test generates a surface wave in the layer, which spectral analysis points out the modulus lowering.

A chemical ageing is also applied to the second series of prisms. They were immersed in an ammonium nitrate solution (450 g/l) for 90 days. The specimens are partially sealed, so that only one 150×300 mm side is submitted to the solution. The degradation is observed using different techniques. Mercury permeability and water porosity measurements were performed [11]. Table 2 shows the porosity evolution with depth. The values are averaged on 10 mm thick slices and do not account for a higher local porosity, which locates near the exposed side of the samples [12].

3. Theoretical background

3.1. Transversely isotropic model

The ageing process of the specimens provides obviously a layered structure parallel to the 150×300 mm side. Hence, a globally transversely isotropic medium is assumed, referred to the Cartesian coordinate axes $(\vec{1}, \vec{2}, \vec{3})$, with the material symmetry axis $\vec{1}$ (Fig. 2). The Voigt stiffness

Table 2
Density and porosity measurement after chemical ageing

Depth from exposed side	Density	Porosity
0–10 mm	1.85	0.302
10–20 mm	2.10	0.193
20–30 mm	2.16	0.169
Relative error (%)	9	

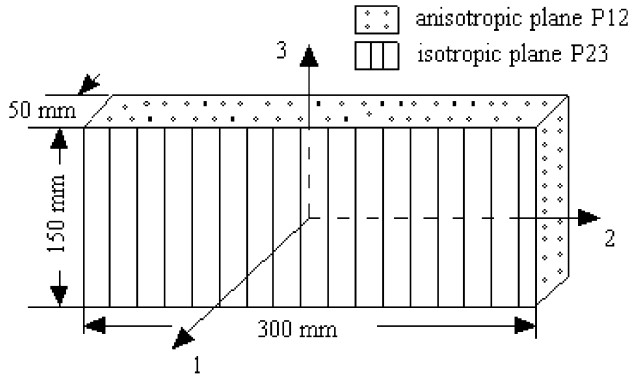

Fig. 2. Microconcrete sample anisotropic solid.

matrix [**C**] reorders the fourth-order stiffness tensor ***C*** to define the stress–strain relationship

$$[\sigma_{11},\sigma_{22},\sigma_{33},\sigma_{23},\sigma_{31},\sigma_{12}]^T = [\mathrm{C}][\varepsilon_{11},\varepsilon_{22},\varepsilon_{33},2\varepsilon_{23},2\varepsilon_{31},2\varepsilon_{12}]^T \quad (1)$$

The following expression of [**C**] holds for the transversely isotropic medium

$$[\mathrm{C}] = \begin{bmatrix} c_{11} & c_{12} & c_{12} & & & \\ c_{12} & c_{22} & c_{23} & & 0 & \\ c_{12} & c_{23} & c_{22} & & & \\ & & & \frac{c_{22}-c_{23}}{2} & & \\ & 0 & & & c_{55} & \\ & & & & & c_{55} \end{bmatrix} \quad (2)$$

The boundary conditions of the samples provide during the ageing a dependence of the mechanical properties with the x_1 coordinate mainly (Fig. 3). Hence, the sample can be modelled as a sequence of homogeneous isotropic layers parallel to the plane P23. It induces an equivalent homogeneous transversely isotropic medium. In the long wave limit, the elasticity coefficients are classically computed in geophysical engineering, as given by Backus [13]

$$c_{11} = \left\langle \frac{1}{\lambda+2\mu} \right\rangle^{-1}, c_{13} = \left\langle \frac{1}{\lambda+2\mu} \right\rangle^{-1} \left\langle \frac{\lambda}{\lambda+2\mu} \right\rangle$$

$$c_{23} = \left\langle \frac{2\lambda\mu}{\lambda+2\mu} \right\rangle + \left\langle \frac{1}{\lambda+2\mu} \right\rangle^{-1} \left\langle \frac{\lambda}{\lambda+2\mu} \right\rangle^2$$

$$c_{33} = \left\langle \frac{4\mu(\lambda+\mu)}{\lambda+2\mu} \right\rangle + \left\langle \frac{1}{\lambda+2\mu} \right\rangle^{-1} \left\langle \frac{\lambda}{\lambda+2\mu} \right\rangle^2$$

$$c_{66} = \left\langle \frac{1}{\mu} \right\rangle^{-1}, c_{44} = \langle \mu \rangle \quad (3)$$

where $\langle\cdot\rangle$ denotes the thickness averaging.

To apply Eq. (3), the Lamé coefficients are defined by

$$\lambda(x_1) = \lambda_1 + \sum_{i=2}^{n} (\lambda_i - \lambda_{i-1})\eta(x_1 - x_{1i}) \quad (4)$$

and similarly for $\mu(x_1)$.

$\eta(\cdot)$ stands for the Heaviside function, x_{1i} is the interface abscissa between layers L_{i-1} and L_i and λ_i and μ_i are the Lamé constants of the ith layer.

The relationship between the Lamé coefficients and the porosity ε calls for the material homogenization. This has been studied by many authors. For example, Kachanov [14] derived explicit formula

$$E = \frac{E^{(0)}}{1 + \frac{16[1-\nu^{(0)2}][1-0.3\nu^{(0)}]}{9[1-0.5\nu^{(0)}]}\varepsilon}$$

$E^{(0)}$ and $\nu^{(0)}$ define the Young modulus and Poisson ratio of the uncracked medium. Generalization was performed to account for anisotropy and cracks mechanical interaction. The influence of the porosity geometrical anisotropy about the elastic properties has been also widely investigated. Finite element method and differential schemes based, for example, on a periodic media hypothesis [15] provide the elasticity constants of aerated concretes.

The wave scattering theory is another way to investigate the homogenization problem. It is used in connection with the ultrasonic inspection developed in our study.

Assuming an isotropic dilution of ellipsoidal penny cracks, λ_i and μ_i are computed by the perturbation method of the Hudson [9] homogenization analysis. It is available for wavelength much longer than the radii and separation distance of the cracks and provides expressions up to the second order of the porosity parameter ε. For writing

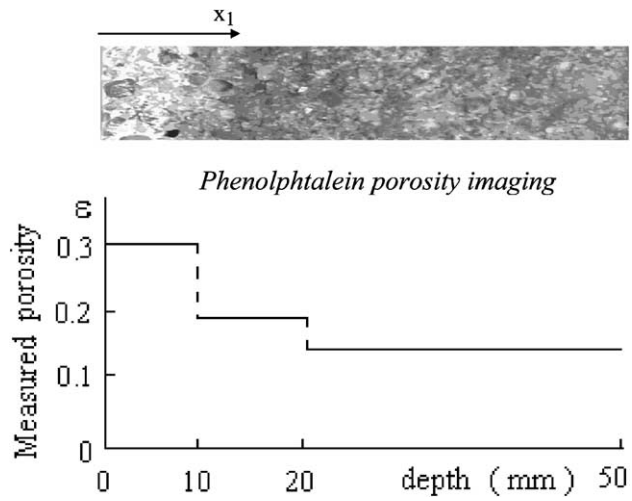

Fig. 3. Chemical ageing porosity profile.

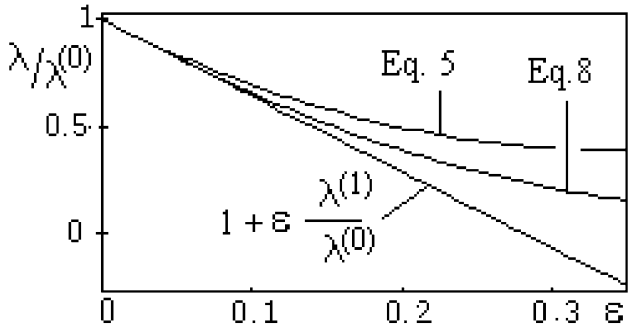

Fig. 4. Lamé coefficient λ versus porosity.

convenience related to *i*th layer, index *i* will be skipped. Expanded Lamé constants are

$$\lambda = \lambda^{(0)} + \varepsilon\lambda^{(1)} + \varepsilon^2\lambda^{(2)},\ \mu = \mu^{(0)} + \varepsilon\mu^{(1)} + \varepsilon^2\mu^{(2)} \tag{5}$$

The terms of order zero are related to the ideally uncracked medium and the perturbation terms induced by the wave scattering on the cracks are

$$\mu^{(1)} = -\frac{2}{15}\mu^{(0)}(3U_t + 2U_1),\ \frac{3\lambda^{(1)} + 2\mu^{(1)}}{3\lambda^{(0)} + 2\mu^{(0)}} = -\frac{3\lambda^{(0)} + 2\mu^{(0)}}{3\mu^{(0)}}U_1,$$

$$\mu^{(2)} = \left(\frac{2}{15}\right)^3 \mu^{(0)}\frac{3\lambda^{(0)} + 8\mu^{(0)}}{\lambda^{(0)} + 2\mu^{(0)}}(3U_t + 2U_1)^2,$$

$$\frac{3\lambda^{(2)} + 2\mu^{(2)}}{3\lambda^{(0)} + 2\mu^{(0)}} = \frac{(3\lambda^{(0)} + 2\mu^{(0)})^3}{27\mu^{(0)}(\lambda^{(0)} + 2\mu^{(0)})}U_1^2 \tag{6}$$

Eq. (6) involve the discontinuity factors U_t and U_l of the wave displacement field across the cracks. Applying the analysis of Eschelby [16] induces the expressions

$$\text{transverse discontinuity} : U_t = \frac{16}{3}\frac{1-\nu^{(0)}}{2-\nu^{(0)}}(1+M)^{-1} \tag{7}$$

$$\text{longitudinal discontinuity} : U_1 = \frac{8}{3}(1-\nu^{(0)})(1+K)^{-1}$$

The shear coefficient and bulk coefficients

$$M = [(4/\pi)((1-\nu^{(0)})/(2-\nu^{(0)}))]\kappa_g$$

$$K = (2/3\pi)(1-\nu^{(0)})[4\kappa_g - (3\kappa_a/(S_r(1-r)-1))]$$

range from zero to high values, according to whether the cracks are open or filled with a rigid material. Consequently, the mechanical behaviour of the cracks is adjusted with four coefficients, which call for the geometrical aspect (radius *a* and thickness *c*) and the mechanical properties (shear modulus μ, bulk modulus $\bar{k}_a$ of the filling material and bulk modulus $\bar{k}_w$ of the water contained).

These coefficients are (1) the crack bulk moduli ratio $r = \bar{k}_a/\bar{k}_w$, (2) the saturation degree $0 < S_r < 1$ and (3) the reduced moduli $\kappa_g = (a/c)(\mu/\mu^{(0)})$ and $\kappa_a = (a/c)(\bar{k}_a/\mu^{(0)})$.

For a practical point of view, we derive from the series approximation (Eq. (5)) a phenomenological law, which can be used for the layer highest porosities (Fig. 4) and is relevant for the study. It is done by means of hyperbolic functions, which avoid to increase the polynomial degree when ε grows and provide the constant lowering with the porosity

$$\lambda = \lambda^{(0)}\left[1 + \mathrm{Th}\left(\frac{\lambda^{(1)}}{\lambda^{(0)}}\varepsilon\right)\right],$$

$$\mu = \mu^{(0)}\left[1 + \mathrm{Th}\left(\frac{\mu^{(1)}}{\mu^{(0)}}\varepsilon\right)\right] \tag{8}$$

3.2. Stiffness identification scheme

The problem of plane wave propagation in continuous media, with density ρ and stiffness tensor $\mathbb{C}$ reordered in vector $\boldsymbol{C}$, shows classically [17] that the speed of propagation V in direction $\vec{n}$ verifies the Christoffel characteristic equation

$$f(\mathbf{C}, \rho V) = \left|\mathbb{C} : (n \otimes n) - \rho V^2 I\right| = 0 \tag{9}$$

where $|\cdot|$ is the determinant notation, I is the identity matrix, $\otimes$ is the tensorial product and (:) is the double contracted tensorial product. Eq. (9) provides an overdetermined system of N nonlinear equations, as n_k and V_k are given data obtained by N experiments. Because ρ, n_k and V_k are experimental values, Eq. (9) is not exactly verified. The accuracy in a probabilistic sense results from the statistical distribution of the errors on $\boldsymbol{C}$.

Noting the error vector

$$\widetilde{\mathscr{F}} = \{f(\widetilde{\boldsymbol{C}}, \rho V_k) : k = 1, \ldots, N\} \tag{10}$$

the best approximation $\tilde{\boldsymbol{C}}$ of the tensor $\boldsymbol{C}$ minimizes the functional

$$\varphi(\widetilde{\boldsymbol{C}}) = \left\|\widetilde{\mathscr{F}}\right\|^2 \tag{11}$$

Setting the error vector $\boldsymbol{R} = \widetilde{\boldsymbol{C}} - \boldsymbol{C}$ and linearizing the error, one obtains

$$e_k = f(\widetilde{\boldsymbol{C}}, \rho V_k) - f(\boldsymbol{C}, \rho V_k) = \frac{\partial \widetilde{\mathscr{F}}_k}{\partial \boldsymbol{C}}\boldsymbol{R} \tag{12}$$

Inverting Eq. (12) extracts the error vector [18]

$$\boldsymbol{R} = \left\{\left[\frac{\partial \widetilde{\mathscr{F}}}{\partial \boldsymbol{C}}\right]^T \frac{\partial \widetilde{\mathscr{F}}}{\partial \boldsymbol{C}}\right\}^{-1}\left[\frac{\partial \widetilde{\mathscr{F}}}{\partial \boldsymbol{C}}\right]^T e \tag{13}$$

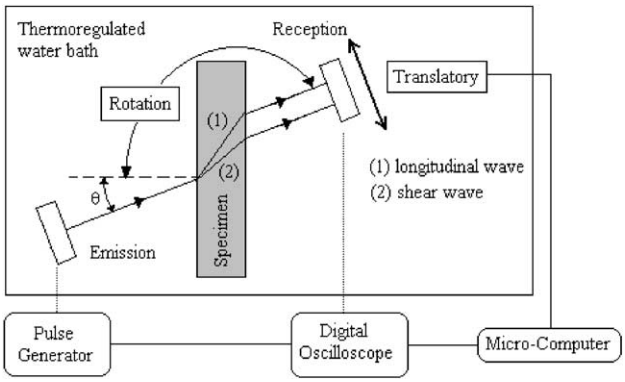

Fig. 5. Ultrasonic tank principle (Tests T1 and T2).

The statistical approach [19] provides the accuracy interval on a component of $\boldsymbol{C}$

$$\widetilde{C}_i - \Delta(C_i) \le C_i \le \widetilde{C}_i + \Delta(C_i) \tag{14}$$

$\Delta(\boldsymbol{C}_i)$ is the confidence interval of the stiffness coefficient $\boldsymbol{C}_i$. It deducts from the covariance matrix $\boldsymbol{\Phi}$ of $\boldsymbol{R}$

$$\Delta(C_i) = \vartheta\sqrt{\Phi_{ii}} \tag{15}$$

Number ϑ in Eq. (15) corresponds with a 90% probable confidence interval $\Delta(\boldsymbol{C}_i)$. The Student law of ϑ is chosen, matching the random variable $\frac{R_i}{\sqrt{\Phi_{ii}}}$ distribution, deducted from the experiments.

4. Experimental analysis

4.1. Laboratory equipment

The tank ultrasonic facility (Fig. 5) uses two broadband transducers immersed in 30 ± 0.1 °C temperature-controlled water. The receiver transducer is moved by a precision mechanical translator for taking the wave beam shift into account. The angle of the sample is monitored by a goniometer, which holds the sample between the 250 kHz transducers. The propagation in various direction is studied, and the temporal response of the receiver is filtered numerically. Both times of flight and amplitudes are relative to a reference signal acquired and stored without the sample. Under these conditions, the assumptions of harmonic plane wave are well justified, providing the best identification of the mechanical coefficients.

The impact laser device (Fig. 6) is a pulsed source. A cylindrical or a spherical lens focuses the radiated electromagnetic energy, which is adjustable from 0.060 to 0.250 J on the sample, providing a thermoelastic or ablation wave generation on the interface. The detection on the back face of the specimen is provided with a laser heterodyne probe measuring the nanometer displacement order of the transmitted wave. The surface wave travelling on the generation interface is observed, setting the probe

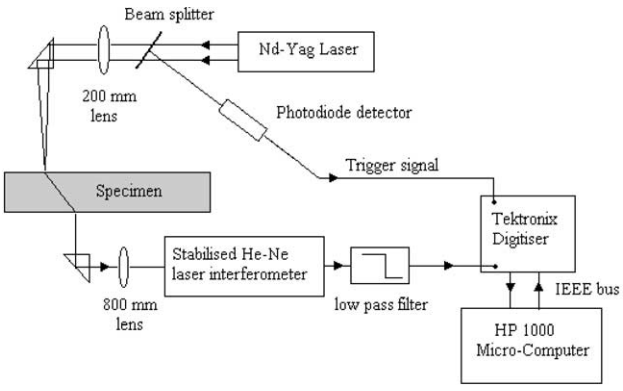

Fig. 6. Impact laser principle (Test T3).

Table 3
T1 immersed unsealed samples (GPa)

	c_{11}	c_{12}	c_{22}	c_{23}	c_{55}
Initial	48.5 ± 0.7	14.5 ± 1.2	51.7 ± 2.8	13.4 ± 2.2	17.1 ± 0.6
Freeze	42.4 ± 0.6	10.9 ± 0.9	40.3 ± 2.2	6.1 ± 1.0	15.3 ± 0.5
Chemical	37.8 ± 0.5	7.1 ± 0.6	35.9 ± 2.0	2.3 ± 0.4	14.8 ± 0.5

Table 4
T2 immersed sealed samples (GPa)

	c_{11}	c_{12}	c_{22}	c_{23}	c_{55}
Initial	39.6 ± 0.6	7.2 ± 0.6	40.3 ± 2.2	6.3 ± 1.0	15.8 ± 0.5
Freeze	35.8 ± 0.5	8.3 ± 0.7	36.5 ± 2.0	5.8 ± 1.0	12.6 ± 0.4
Chemical	18.0 ± 0.3	0.4 ± 0.1	25.7 ± 1.4	6.8 ± 1.1	11.3 ± 0.4

Table 5
T3 laser test (GPa)

	c_{11}	c_{12}	c_{22}	c_{23}	c_{55}
Initial	43.5 ± 0.6	10.0 ± 0.9	45.4 ± 2.5	11.4 ± 1.9	15.6 ± 0.5
Freeze	35.8 ± 0.5	14.2 ± 1.2	33.3 ± 1.8	2.6 ± 0.4	10.8 ± 0.4
Chemical	21.4 ± 0.3	1.5 ± 0.1	21.2 ± 1.2	2.4 ± 0.4	9.4 ± 0.3

Table 6
Measured porosity, density and Rayleigh speed

Ageing	Initial	Freeze	Side chemically	
			Unaltered	Altered
Speed (m/s)	2480	1700	2325	1500
ε	0.169	0.22[a]	0.169	0.302
ρ (kg/m^3)	2.16	2.00	2.16	1.85

[a] Not measured but assumed value in the 3 mm layer.

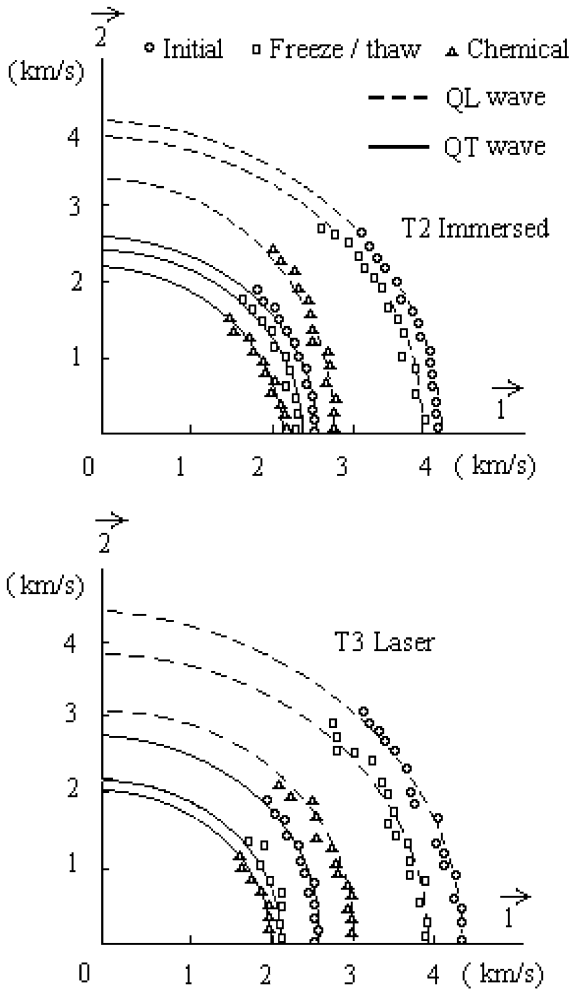

Fig. 7. Wave group velocity.

and the source on the same side. A translation of the lens and mirrors is used to make experiments at different angles of the wave propagation within the laminate. A rotation of the sample can be monitored to investigate distinct planes of anisotropy.

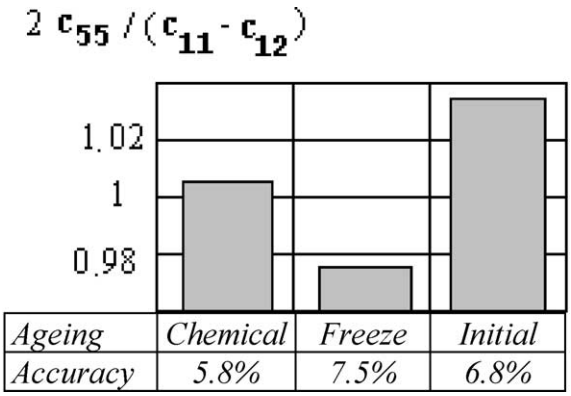

Fig. 8. Anisotropy factor.

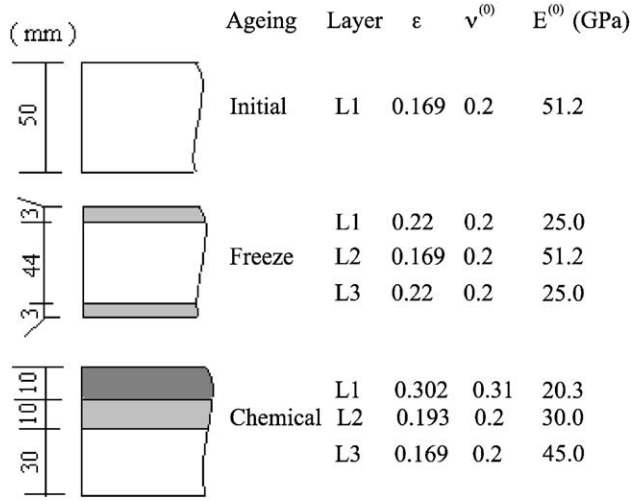

Ageing	Layer	ε	$\nu^{(0)}$	$E^{(0)}$ (GPa)
Initial	L1	0.169	0.2	51.2
Freeze	L1	0.22	0.2	25.0
	L2	0.169	0.2	51.2
	L3	0.22	0.2	25.0
Chemical	L1	0.302	0.31	20.3
	L2	0.193	0.2	30.0
	L3	0.169	0.2	45.0

Fig. 9. Multilayer models.

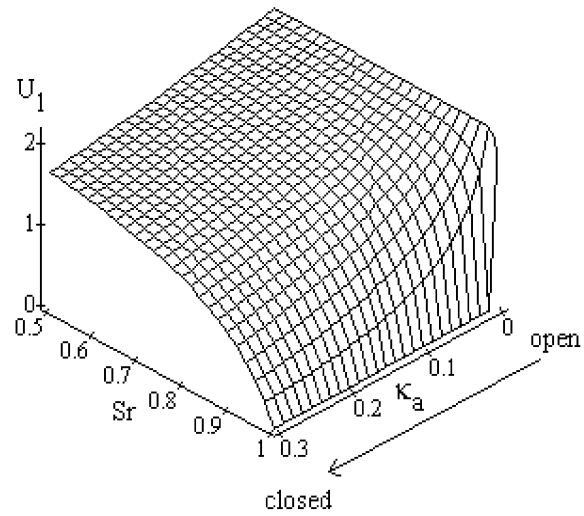

Fig. 10. Crack sensitivity to air bulk modulus and saturation degree.

Table 7
Parameter fitting from Table 6 measurements

Ageing	Initial	Freeze	Side chemically	
			Unaltered	Altered
$\mu^{(0)}$ (GPa)	21.3	10.4	18.8	7.8
$\lambda^{(0)}$ (GPa)	14.2	6.9	12.5	12.6
$\nu^{(0)}$	0.2	0.2	0.2	0.31
$E^{(0)}$ (GPa)	51.2	25.0	45.0	20.3

Table 8
Saturation degree S_r (assumed values)

Test	T1			T2 and T3
Layer	L1	L2	L3	L1–L3
Initial	1	–	–	0.2
Freeze	1	1	–	0.2
Chemical	1	1	1	0.2

4.2. Experimental identification

Three types of experiments are done to identify the stiffness c_{ij}. Wave incidence angle range is between 0° and 45°. They referred to the following:

T1: Ten unsealed samples were immersed for 5 days. Near saturation, they were submitted to transmission ultrasonic tests.
T2: Same as T1, but the samples are sealed with a hydrophobic silicon film and tested immediately, avoiding the water penetration. Comparison with T1 indicates the water content influence on the identification of the stiffness constants.
T3: Laser method on a single dry sample completed with the Rayleigh wave speed measurement.

On unsaturated samples, ultrasonic test T2 and laser test T3 evolution in the P12 plane of the transmitted waves group velocities are plotted in Fig. 7. The comparison is done between the initial state and the damaged samples, showing a significant bulk wave velocity lowering with the alteration level. The anisotropy factor is close to unity (Fig. 8). This proves that the hypothesis of a local isotropic stiffness, which derives from the randomly oriented crack assumption, is relevant. The mean values of the stiffness coefficients, homogenized over the thickness of the specimens (Tables 3–5), are not very sensitive to the anisotropy due to the porosity gradient. The modelling will indicate that the involved layered structures can globally look isotropic (Tables 9 and 10). Such result agrees with the work of Cabrillac and Malou [15], which shows that the mechanical anisotropy of a cracked material is a consequence of the porosity geometrical anisotropy, coming from a polarization of the crack orientation.

Tables 3 and 4 report the stiffness mean values obtained on 10 samples of each aged state. They indicate that the microconcrete water content plays a significant influence on the behaviour. The T1 test provides higher stiffness values than the T2. This is because the bulk wave speed is higher in the saturated specimens of the T1 experiments and induces correspondingly high stiffness. The sealed specimens of the T2 test provide lower microconcrete stiffness values and match with the laser T3 tests, involving a similarly small water content (Table 5).

To take advantage of the laser equipment, the Rayleigh wave speed is measured (Table 6). The laser heterodyne receiver is set on the same side as the laser impact source. It provides simple operating condition to investigate the superficial layers of the laminates. Referencing to the initial state and the chemically aged unaltered side of the samples, the generation and the detection of the Rayleigh wave is efficiently achieved. It demonstrates the interest of a method without contact to investigate new approaches of concrete identification.

5. Ageing modelling

An application of the transversely isotropic model issued from the Backus and Hudson theories checks if a porous elastic medium makes sense with the propagation of the waves in the microconcrete composite material. This approach is qualitative to determine magnitude orders of the porosity and elastic constants. It is because the homogenization theory of Hudson coupled with the Backus averaging analysis can be used as an investigation only, according to the simplified schemes they involve. A refined fitting would require a more accurate analysis of the sample physical influence. The consequence on the ultrasonic behaviour modelling would involve a specific work, out of our initial objective.

Hence, the following analysis assumes layered laminates (Fig. 9), which elastic moduli are determined to match with the measured Rayleigh wave speed, accurately approximated [20] by

$$V_R = \frac{0.87 + 1.12}{1 + \nu}\sqrt{\frac{\mu}{\rho}} \tag{16}$$

It is necessary to estimate relevant physical magnitude orders of the parameters, which are not directly measured. The layers are permeated with voids partially filled with air and water, which bulk moduli ratio is $r = 10^{-4}$. Air and water filling induces a vanishing crack shear modulus $\kappa_g = 0$ and a very low bulk modulus $\kappa_a = 0.001$. The saturation degree (Table 8) of the sample laser T3 tests, immersed but protected from water absorption T2 tests, is chosen as $S_r = 0.2$. Then, Eqs. (5)–8) and (16) derive the Lamé coefficients $\lambda^{(0)}$ and $\mu^{(0)}$, the Young modulus $E^{(0)}$ and the Poisson ratio $\nu^{(0)}$ of the uncracked medium (Table 7). The hypothesis of open cracks is justified by the sensitivity of the identified stiffness to the water content (Table 8). The chemically aged specimens, involving the highest porosity, behave very differently according to the water absorption condition ($S_r \sim 1$, Table 3; $S_r \sim 0.2$, Table 4).

The air compressibility within the crack induces very low values of the reduced bulk modulus κ_a. Hence, a high saturation is necessary to modify the function U_1 (Fig. 10). This may explain why the water content influence on ultrasonic measurements is until now a debated and difficult topic.

The simulated stiffness values at Tables 9 and 10 agree with the experimental identification shown at Tables 3 and 4. It is of interest to observe that this result is obtained by

Table 9
T1 layered model (GPa)

	c_{11}	c_{12}	c_{22}	c_{23}	c_{55}
Initial	49.7	14.5	49.7	14.5	17.6
Freeze	43.7	12.8	46.3	13.4	16.5
Chemical	33.1	10.9	36.0	11.2	12.4

Table 10
T2 layered model (GPa)

	c_{11}	c_{12}	c_{22}	c_{23}	c_{55}
Initial	37.5	5.6	37.5	5.6	16.0
Freeze	32.3	4.7	34.9	5.1	14.9
Chemical	21.2	2.8	25.9	3.5	11.2

keeping the initial Lamé constants values of the unaged specimens for the solid skeleton of the freeze/thaw samples, except in a very thin superficial layer where the relative modulus Byggforsk laboratory measurement is confirmed, involving a decreasing of the Young modulus $E^{(0)}$ neighbouring 50%. Moreover, the cracking at the microscopic scale, induced by the freeze/thaw exposure, is active in the superficial layers, but the scaling effect is absent more deeply, where such freeze/thaw cracks behave closed for the considered wavelength.

On the contrary, during the chemical transformation, the Portland phase of the cement vanishes and the hydrated calcium silicate structure is modified. This may explain that the skeleton moduli differ in altered L1 and L2 layers of the chemically aged samples (Fig. 9 and Table 7). The superficial layer L1 should soften ($E \sim 20.3$ GPa) and become less compressible ($\nu \sim 0.3$) than the unaltered part of the specimens.

6. Conclusion

The immersed ultrasonic and impact laser methods were applied to separate increasing ageing levels of microconcrete specimens. Both of them identify the magnitude order of the matrix stiffness coefficients. However, the identification method is not yet updated, especially to take into account the local heterogeneity profile of the material. Considering the altered sample as an equivalent homogenized transversely isotropic material looks a rough hypothesis to ensure appropriately the physical acoustic ray propagation within the heterogeneous medium. This induces an incomplete knowledge of the modelling scheme and can induce an erroneous wave speed evaluation. Furthermore, the diffusion of the waves on aggregates, pores and cracks must be implemented in a more elaborated model, accounting for a better definition of the propagation physics. Then, it would become possible to work with smaller wavelength, a condition to investigate the altered superficial layers. Consequently, the Backus thickness averaging model, accounting for the porous elastic medium analysis of Hudson, provides only magnitude orders to confirm the main softening trends of the observed alterations. The first results obtained from a pulsed laser generated Rayleigh wave indicate that the local variation of the elastic properties should be included within the analysis of the ultrasonic inspection method. To extend the investigation of the acoustic ray propagation in a continuously heterogeneous structure is a future objective of the research development to identify the damaged superficial layer of aged concretes.

Acknowledgements

The authors thank EDF R&D for support (Contract no. C56664) and S. Jacobsen of Norway Byggforsk laboratory.

References

[1] B. Gérard, Contribution des couplages mécaniques-chimie-transfert dans la tenue à long terme des ouvrages de stockage de déchets radioactifs. Thesis, LMT ENS Cachan, 1996.
[2] S. Jacobsen, Scaling and cracking in unsealed freeze/thaw testing of portland cement and silica fume concrete. Thesis, Trondheim University, 1995.
[3] Y. Berthaud, Damage measurement in concrete via an ultrasonic technique, Cem. Concr. Res. 21 (1991) 219–228.
[4] Y. Berthaud, Mesures et modélisation de l'endommagement des matériaux. Report, LMT ENS Cachan, 1991.
[5] B. Hosten, S. Baste, Ultrasonic evaluation of anisotropic damage induced in glass/epoxy composites by water immersion, Rev. Prog. Quant. Nondestruct. Eval. 11 (1992) 1539–1548.
[6] Y. Bamberger, J.J. Marigo, G. Cannard, Microfissuration du béton et propagation d'ondes ultrasonores, Proc. Eur. Col. 115 295 (1979) 715–734.
[7] M. Deschamps, Reflection and refraction of the inhomogeneous plane wave, World Sci. 5 (1994) 164–206.
[8] M. Deschamps, C. Bescond, Numerical method to recover the elastic constant from ultrasound group velocities, Ultrasonics 33 (1995) 205–211.
[9] J.A. Hudson, Overall properties of a cracked solid, Math. Proc. Camb. Philos. Soc. 88 (1975) 371–384.
[10] S. Jacobsen, 1999. Freeze/thaw cracking of w/c = 0.5 prisms. Report 9526, Byggforsk, Norway.
[11] N. Rafai, Détermination du profil de porosité dans un mortier ayant été soumis à une lixiviation par du nitrate d'ammonium. Report 00.4891.001.01A, LERM, 2000.
[12] C. Le Bellégo, B. Gérard, G. Pijaudier Cabot, Chemo-mechanical effects in mortar beams subjected to water hydrolysis, ASCE, J. Eng. Mech. (2000) 266–272.
[13] G.E. Backus, Long-wave elastic anisotropy produced by horizontal layering, J. Geophys. Res. 67 (11) (1962) 4427–4440.
[14] M. Kachanov, Elastic solids with many cracks and related problems, Adv. Appl. Mech., vol. 30, Academic Press, 1993.
[15] R. Cabrillac, Z. Malou, Mechanical modelization of anisotropic porous material with a homogenization method. Application to aerated concretes, Constr. Build. Mater. 14 (2000) 25–33.
[16] J.D. Eschelby, The determination of the elastic field of an ellipsoidal inclusion, and related problems, Proc. R. Soc. A241 (1957) 376–396.
[17] B. Audoin, Estimation de l'intervalle de confiance des constantes d'élasticité identifiées à partir des vitesses de propagation ultrasonores, C. R. Acad. Sci. Paris, Ser. 2 (1991) 679–686.
[18] A. Gourdin, M. Boumahrat, Méthodes numériques appliquées, Lavoisier, Paris, 1983.
[19] M. Walpole, M. Myers, Probability and statistics for engineers and scientists, 2nd ed., Collier MacMillan, 1978.
[20] B.A. Auld, Acoustic fields and waves in solid, 2 (1990).